

Supporting Information

Dissolution and Performing Homogeneous Photocatalysis of Polymeric Carbon Nitride

Chaofeng Huang,^{§†} Jing Wen,^{§‡} Yanfei Shen,[†] Fei He,[†] Li Mi,[†] Ziyu Gan,[†] Jin Ma,[†]
Songqin Liu,[†] Haibo Ma,^{‡*} Yuanjian Zhang^{†*}

[†]Jiangsu Engineering Laboratory of Smart Carbon-Rich Materials and Device, Jiangsu Province Hi-Tech Key Laboratory for Bio-Medical Research, School of Chemistry and Chemical Engineering, Medical School, Southeast University, Nanjing 211189, China,
Email: Yuanjian.Zhang@seu.edu.cn

[‡]School of Chemistry and Chemical Engineering, Nanjing University, Nanjing 210023, China, Email: haibo@nju.edu.cn

[§] These authors contributed equally to the work

Table of Contents

Entry	Page
Experimental Procedures	S4-5
Characterization	S6
Computational methods	S7
More discussion of the maintenances of the chemical structure of the bulk CN before and after the dissolution in MSA	S8
Characterization of the starting bulk CN	
Fig. S1 The proposed successive thermal condensation of dicyandiamide into the heptazine-based bulk CN that was used in this study	S9
Fig. S2 XRD patterns of DCDA, melamine, melem, melon, bulk CN and that recovered from the CN solution by precipitation using poor solvents (r-CN)	S10
Fig. S3 FT-IR spectra of DCDA, melamine, melem, melon, bulk CN and r-CN	S11
Fig. S4 SEM image of the bulk CN	S12
More evidences of the dissolution of CN in MSA	
Fig. S5 Photo of the bulk CN powders gradually dissolves in the solvent MSA without stirring before and after 5 days	S13
Fig. S6 (a) Photograph of CN nanosheets dispersion in water (left, 0.1 mg/mL) and the CN solution in MSA (right, 50 mg/mL) at room temperature, and irradiated by using a red laser pointer. (b) The particle size distribution of CN in MSA tentatively evaluated by dynamic light scattering (DLS, $\lambda=640$ nm)	S14
Supplementary proofs for the recovery of CN by precipitation using poor solvents	
Fig. S7 UV-Vis spectra of bulk CN powder and r-CN	S15
Fig. S8 PL spectra of the starting CN and r-CN	S16
Fig. S9 N ₂ adsorption-desorption isotherm curves of bulk CN and r-CN. Inset shows the pore volume and BET surface area	S17
Table S1 Elemental analysis of bulk CN and r-CN	S18
Supplementary data for photocatalytic dehydrogenation of TMB and N-demethylation of AB	
Fig. S10 Proposed mechanism of photocatalytic oxidation of TMB	S19
Fig. S11 UV-vis absorption spectra of the reaction mixture for the dehydrogenation of TMB using CN-hetero and CN-homo photocatalysts at different reaction time	S20
Fig. S12 Absorbance of TMB _{ox} at 456 nm as a function of time during photocatalytic dehydrogenation using MSA and CN-homo catalyst	S21
Fig. S13 The turnover frequency using CN-hetero and CN-homo photocatalysts for dehydrogenation of TMB	S22
Fig. S14 Proposed mechanism of photocatalytic oxidation of Azure B	S23

Fig. S15 UV-vis absorption spectra of the reaction mixture for the N-demethylation of AB using CN-hetero and CN-homo photocatalysts at different reaction time	S24
Fig. S16 Gas chromatography spectra of standard O ₂ , standard CO ₂ , and the gaseous products of photocatalytic N-demethylation of AB by using CN-homo	S25
Fig. S17 Plot of ln(C ₀ /C) as a function of irradiation time for the N-demethylation of AB using CN-hetero and CN-homo photocatalysts	S26
Fig. S18 The XRD patterns of r-CN that was obtained from CN-homo after photocatalytic oxidation of AB using ether as the poor solvent	S27
Table S2 Comparison of the catalytic dehydrogenation activity of TMB using different catalysts	S28
Table S3 Comparison of the catalytic N-demethylation of AB using different catalysts	S29
Supporting references	S30-31

Experimental Procedures

Reagent

Dicyandiamide (DCDA, 99%, Sigma-Aldrich), concentrated sulfuric acid (H_2SO_4 , 95-98%, Sinopharm chemical Reagent), methanesulfonic acid (MSA, 99.5%, Aladdin), Chlorosulfonic acid (ClSA, 99%, Energy Chemical), Ethyl methyl sulfonate (EMS, 99%, Aladdin), Azure B (AB, 90%, J&K), 3,3',5,5'-tetramethylbenzidine (TMB, Aladdin) were used without further purification. All other reagents were of analytical grade and used as received unless otherwise specified. Ultrapure water ($18.2 \text{ M}\Omega\cdot\text{cm}$) was obtained from a Smart2 water purification system (Thermo Scientific, USA).

Preparation of CN

CN was prepared by heating dicyandiamide for 4 hours to $550 \text{ }^\circ\text{C}$ and kept at this temperature for 4 hours in air. The final product was ground into fine powder with sizes of several micrometers before use.

Preparation of different CN solution

The CN solution (50 mg/mL) was obtained by stirring the mixture of CN (500 mg) and 10 mL MSA, H_2SO_4 , ClSA or EMS at room temperature for 10 hours. The concentration of CN in MSA could be up to 200 mg/mL at room temperature. At higher concentration, it becomes very viscous and the exact solubility was difficult to be quantified. Notably, MSA was used to exfoliate other 2D materials, such as hexagonal boron nitride¹ and graphene nanosheets², but not to dissolve them.

Precipitated CN from CN solution

CN powder could be recovered from CN solution by adding some poor solvents (e.g., methanol, acetonitrile, or ether) to initiate the precipitation, washing with the same solvent and lastly H_2O , and freeze drying. The as-obtained CN powder was denoted as r-CN. Unless otherwise specified, all r-CN in this work was recovered using acetonitrile as the poor solvent with a collection yield of ca. 40%. Moreover, it should be noted that water could be used as a green solvent to exfoliate CN into nanosheets and disperse them. While in regard of dissolving, water was a poor solvent with respect to MSA. Nevertheless, it was suggestive to improve the dispersability of CN nanosheets with

the assistance of MSA during the exfoliation by using water.

Photocatalytic dehydrogenation of TMB

TMB (4.5 mg) and CN-homo (CN dissolved in MSA, 0.5 mg/mL, 30 mL MSA) or CN-hetero (CN dispersed in H₂O, 0.5 mg/mL, 29 mL H₂O+1 mL MSA) were added in a quartz tank (5×5×5cm³), respectively. The reaction system was top-irradiated by using a 300 W Xe lamp (CEL-HXUV300E, China).

Photocatalytic N-demethylation of AB

Firstly, CN-homo (CN dissolved in MSA, 10 mg/mL) or CN-hetero (CN dispersed in H₂O, 10 mg/mL) was added in a quartz tank (5×5×5cm³). Then, AB solution in MSA or water (0.1 mg/mL) was added, respectively. Afterwards, the quartz tank was filled with oxygen by balloon and sealed. Finally, the reaction system was top-irradiated by using a 300 W Xe lamp (CEL-HXUV300E, China).

The recyclability of CN in homogeneous catalysis

Firstly, the CN was separated from the reaction mixture by precipitation and washing with ether for several times. Then, the separated CN solids (10 mg/mL) were dissolved in MSA again (faster than pristine CN due to finer powder) and later mixed with a fresh AB solution (0.1 mg/mL) in 20 mL MSA. After that, the absorbance spectra of the reaction mixture were measured after 3 h. Such procedures were repeated for 3 times.

Characterization

X-ray diffraction (XRD) measurements were undertaken by using SmartLab diffractometer (Rigaku, Japan). The Fourier transform infrared (FT-IR) spectra were carried out on a Nicolet iS10 FT-IR spectrometer (Thermo, USA), equipped with an attenuated total reflection (ATR) setup. The photoluminescence (PL) spectra were performed by fluorescence spectrometer (Fluoromax-4, Horiba Jobin Yvon, Japan). UV-vis absorption spectra were obtained from Cary 100 (Agilent, Singapore) with a diffuse reflectance accessory. Elemental analysis was performed on a Vario EL elemental analyzer (Germany). The size distribution was obtained at a NanoBrook Omni particle size and zeta potential analyzer (Brookhaven Instruments Corporation, USA). Brunauer-Emmett-Teller (BET) surface area and pore volume were calculated from 77 K N₂ adsorption-desorption isotherms by using a NovaWin 1000e instrument (Quantachrome, USA).

Computational methods and results

Adsorption models of single MSA, H₂SO₄, CISA and EMS solvent molecules on CN were studied by quantum chemical calculations. CN nanosheet was modeled by a 5×5×5 trigonal 2-dimensional cluster to compromise the computational cost and accuracy. Firstly, the 5×5×5 trigonal 2-dimensional CN cluster and solvent molecules were optimized, separately. Then, the four adsorbed systems of solvent molecules on CN cluster were optimized. The adsorption energy ($E_{\text{ads-molecule}}$) is calculated by

$$E_{\text{ads-molecule}} = E_{\text{CN+molecule}} - E_{\text{CN}} - E_{\text{molecule}}$$

where $E_{\text{CN+molecule}}$ and E_{CN} are the total energies of the CN cluster with and without adsorbed molecule, respectively. E_{molecule} is the energy of the adsorbed molecule. All equilibrium geometries were optimized by the density functional theory (DFT) with double hybrid M06-2X exchange-correlation functional and 6-31G(d) basis set; meanwhile, the calculations were implemented with polarizable continuum model (PCM) for all systems. All the calculations were carried out by using the Gaussian 09 program.³

As a result, the adsorption energies were calculated by as-described methods and illustrated in this work with an ascending order (-0.84 eV (MSA@CN), -0.73 eV (H₂SO₄@CN), -0.67 eV (CISA@CN), and -0.14 eV (EMS@CN)). Considering the solubility of CN in solvents is determined not only by adsorption energy but also by entropy, the Gibbs free energies have also been obtained by frequency analyses on the four optimized adsorption models, it turned out to be -0.22 eV (MSA@CN), -0.19 eV (H₂SO₄@CN), -0.14 eV (CISA@CN), and 0.33 eV (EMS@CN), respectively. Therefore, the dissolution ability of the solvent molecules in this paper was in accordance with the relative strength of the interaction between solvent molecules and CN, which is the descending order of MSA, H₂SO₄, CISA, and EMS.

More discussion of the maintenances of the chemical structure of the bulk CN before and after the dissolution in MSA

After dissolution, the original chemical structure of the bulk CN was supposed to be not broken down. Firstly, as the direct evidences, the FT-IR and XPS spectra in the main text demonstrated that the major bonding manner of the bulk CN was not significantly altered before and after dissolution, except for the protonation interaction. Moreover, if the decomposition happened, the electronic structure and crystalline of CN would also significantly altered. However, the UV-vis and PL spectra demonstrated that only a very moderate blue-shift was observed, which was also ascribed to the protonation interaction.⁴ Similarly, the XRD patterns of the precipitated CN was most like to that of pristine bulk CN, and quite different to its intermediate species, such as DCDA, melamine, and melem (Fig. S2). Besides, the high collection yield of the CN precipitation from MSA solution (ca. 95%) and the unchanged C/N ratio before and after dissolution by elemental analysis (Table S1) also supported the maintenances of the chemical structure of CN before and after the dissolution in MSA.

Characterization of the starting bulk CN

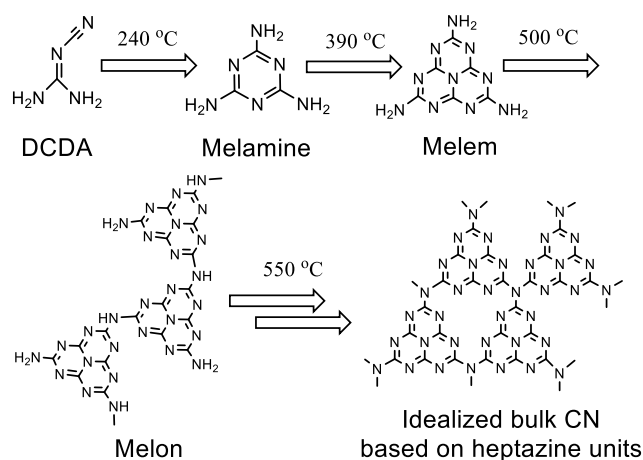


Fig. S1 The proposed successive thermal condensation of dicyandiamide (DCDA) into the heptazine-based bulk CN that was used in this study

The thermal condensation of dicyandiamide (DCDA) at 550 °C that was used in this study has been widely recognized as a facile synthetic pathway to prepare heptazine-unit based polymeric carbon nitride.⁵ TGA measurement in previous report had disclosed that when the polymerization temperature successively increased up to 550 °C, the polymerization degree gradually improved,⁶ and at higher temperature the as-obtained CN would decompose.⁷

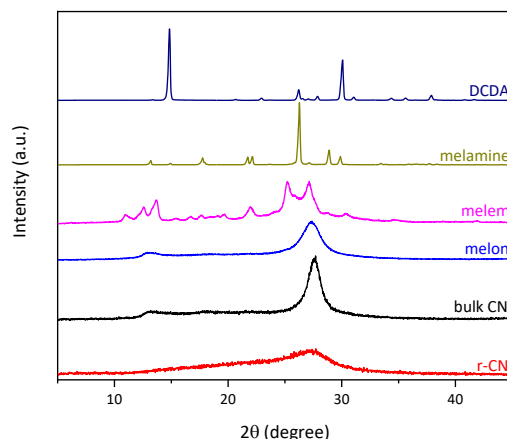


Fig. S2 XRD patterns of DCDA, melamine, melem, melon, bulk CN and r-CN.

The conservation of the stacked framework was studied by X-ray diffraction (XRD). As shown, the representative peak at 27.4° (002) still existed for r-CN, most like that of pristine bulk CN, and quite different to its intermediate species, such as DCDA, melamine, and melem. It supported the fact that the major crystalline structure of CN was retained and the starting bulk CN did not disintegrate after the dissolution and recovered processes.^{4, 8} Nevertheless, it became broader than that of the starting bulk CN powder, along with a much reduced intensity. The low crystallinity mainly resulted from the reduce length of interlayer periodicity due to the precipitation using acetonitrile from poor solvents and the protonation interaction by MSA (see the similar result in protonation of bulk CN using HCl).⁴ In addition, the peak between 10 to 20 degrees was a typical of more oriented CN. Based on the HRTEM result, this peak presumably relates to an in-plane structural packing motif of CN, such as the hole-to-hole distance of the nitride pores in the crystal.⁹ This peak weakens for r-CN showed that an interlayer contribution was contained, either within the distance (then being the distance to the next pore in the next layer) or via the pore regularity (stacked sheets were more flat). Other reasons include that the protonation would make the structure of nitride pores slightly distorted and then the hole to hole distance changed.

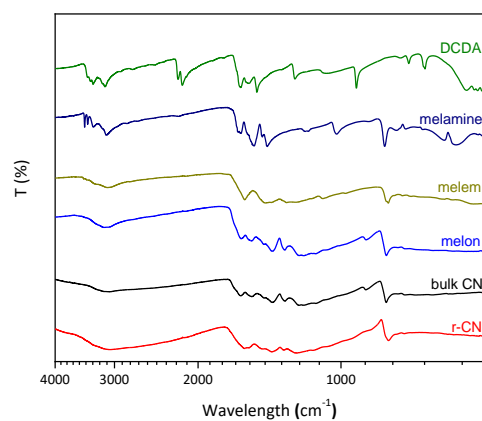


Fig. S3 FT-IR spectra of DCDA, melamine, melem, melon, bulk CN and r-CN.

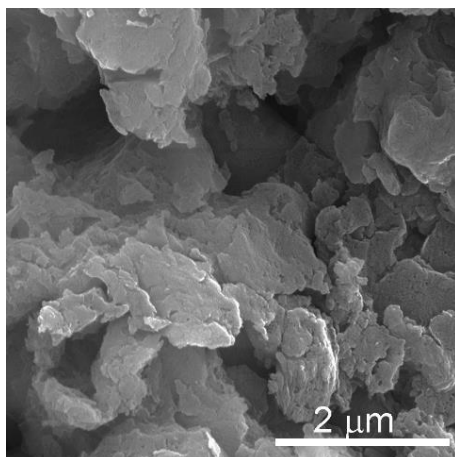


Fig. S4 SEM image of the bulk CN.

More evidences of the dissolution of CN in MSA

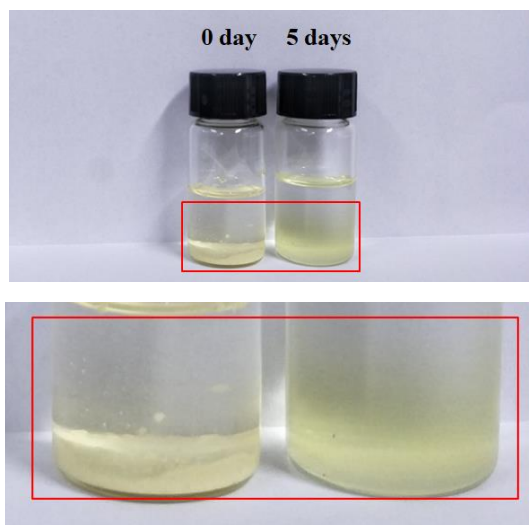


Fig. S5 Photo of the bulk CN powders in the solvent MSA without stirring before and after 5 days.

Upon the careful addition of MSA to CN, the color of the solvent at the bottom of the vial changed after 5 days, as some bulk CN powders dissolved into MSA solvent. It could be persuasive to demonstrate spontaneous dissolution, suggesting the formation of a solution rather than suspension. Nevertheless, notably, the spontaneous dissolution speed was slower than that of high crystallinity PTI·LiBr-based CN by using DMSO,¹⁰ which may be ascribed to different type of bulk CN and the subsequent different kinetics.

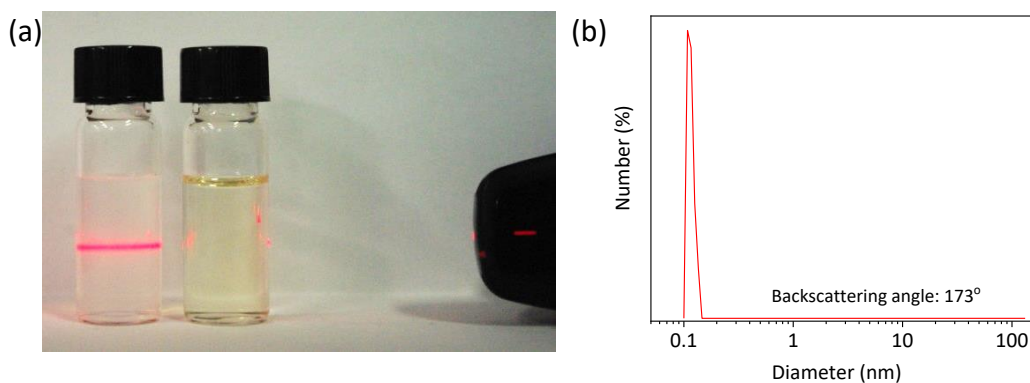


Fig. S6 (a) Photograph of CN nanosheets dispersion in water (left, 0.1 mg/mL) and the CN solution in MSA (right, 50 mg/mL) at room temperature, and irradiated by using a red laser pointer. (b) Particle size distribution of CN in MSA (a preliminary failed measurement) evaluated by dynamic light scattering (DLS, $\lambda=640$ nm).

The Tyndall effect was not observed for CN dissolved in MSA, while that was evident for CN nanosheets dispersion that was obtained by liquid-state exfoliation from the bulk CN according to previous method.¹¹ As the Tyndall effect was negligible by naked eyes using a laser pointer (Fig. S6a), the scattering experiment was further undertaken on a commercial DLS facility which is often used for evaluation of colloids size distribution (Fig. S6b). Due to the potential small particle size of CN in MSA, the backscattering angle of 173° was used for best signal to noise and reproducibility of measurements (see the NanoBrook Omni brochure, URL: <https://www.brookhaveninstruments.com/pdf/Zeta%20Potential/NanoBrook-Omni.pdf>). Unfortunately, the DLS measurement did not give a reliable result, as the sizes were calculated to be smaller than the limit of detection of the instrument (0.3 nm-10 μ m) under the optimized conditions. It should be noted that because the complete solvent parameters of MSA was not available for the DLS measurement, the solvent parameters of water were used alternatively. Nevertheless, although it was failed to measure the size of CN in MSA, as an indirect evidence, it suggested that the sizes of CN in MSA was ultra-small, and was not a typical colloidal system. Therefore, complementary to FT-IR (Fig. S3), XPS (Fig. 1c and Fig. 1d), UV-vis (Fig. S7), PL (Fig. S8), elemental analysis (Table S1) and BET (Fig. S9) characterization, the bulk CN was most presumably dissolved in MSA and formed a true solution as macromolecules with minimal lateral dimensions.

Supplementary proofs for the recovery of CN by precipitation using poor solvents

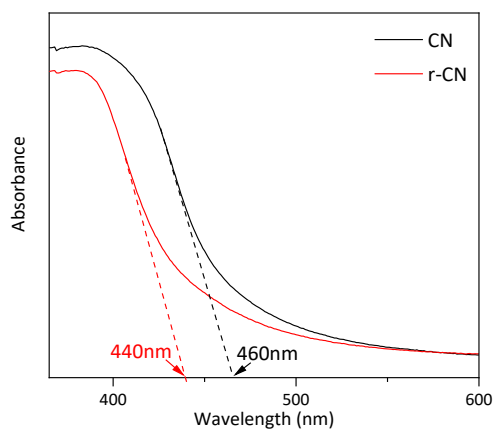


Fig. S7 UV-Vis spectra of the starting bulk CN powder and that recovered from the CN solution by precipitation using poor solvents (r-CN).

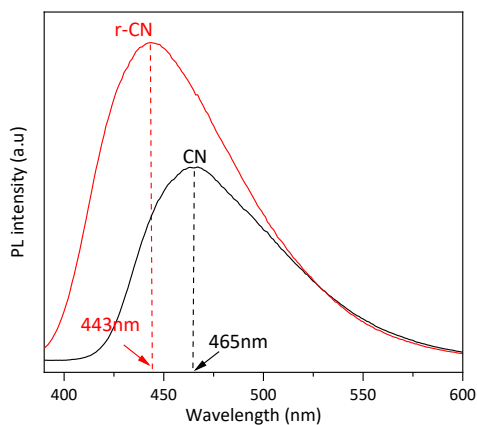


Fig. S8 PL spectra of the starting CN and r-CN ($E_x = 370$ nm)

As shown, the starting bulk CN powder had a maximum PL emission peak at 465 nm, which was originated from the conjugated -C-N- network.⁴ Such emission was slightly blue-shifted to 443 nm for r-CN. The similar phenomenon in the protonation of CN with HCl was also observed.⁴ Thus, the blue-shift of PL spectra herein could be ascribed to the protonation of CN by MSA.

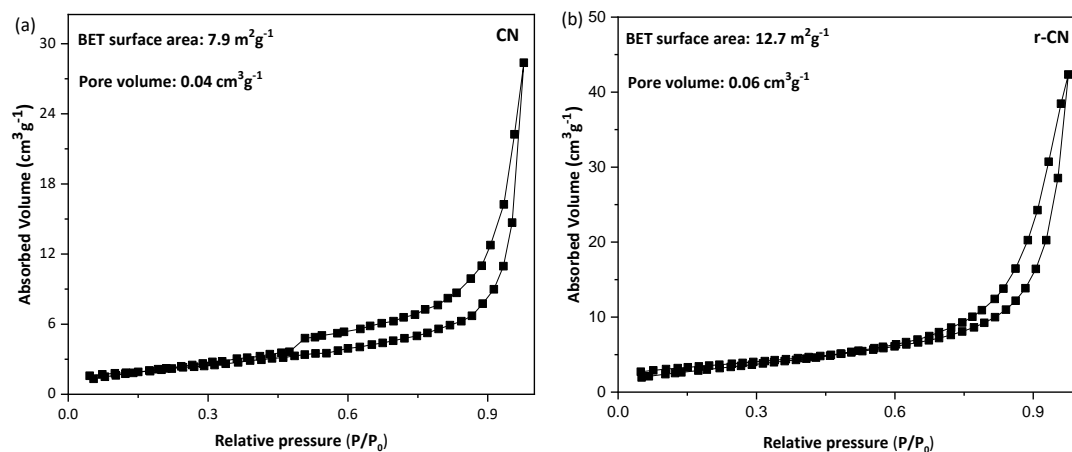


Fig. S9 N_2 adsorption-desorption isotherm curves of the starting bulk CN powder and r-CN. Inset shows the pore volume and BET surface area.

Table S1 Elemental analysis of the starting bulk CN powder and r-CN

	Element (wt. %)		Molar ratio
CN	C	34.93	C/N=0.68
	N	59.52	
	H	2.7	
r-CN	C	29.27	C/N=0.67
	N	50.96	
	H	3.13	

In order to confirm the molar ratio of C/N in the r-CN, the elemental analysis was performed. As shown, the molar ratio of C/N of bulk CN and r-CN were 0.68 and 0.67, respectively. The almost identical C/N ratio supported the facts that the dissolution in MSA did not disintegrate the structure of bulk CN. The amount of H increased for the precipitated CN from MSA solution, which could be explained by a protonation interaction.

Supplementary data for photocatalytic dehydrogenation of TMB and N-demethylation of AB

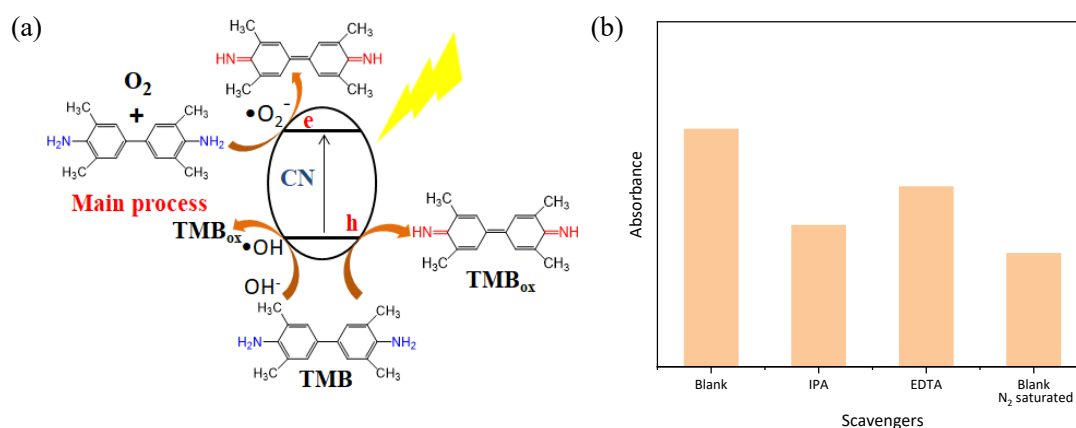


Fig. S10 (a) Proposed mechanism of photocatalytic dehydrogenation of TMB into TMB_{ox}¹². (b) The activity changes of dehydrogenation of TMB by homogeneous CN in MSA after adding isopropanol (IPA, 0.1 mM) and ethylenediamine tetraacetic acid disodium salt (EDTA, 0.1 mM) as scavengers to remove the potential •OH and h⁺, respectively, during the photooxidation reaction.¹³ Due to the interference of p-benzoquinone (BQ) for TMB concentration evaluation, N₂ saturated solution was tested for •O₂⁻. The more evidently decreased activity by removing O₂ in the reaction showed •O₂⁻ was the major species of the reaction.

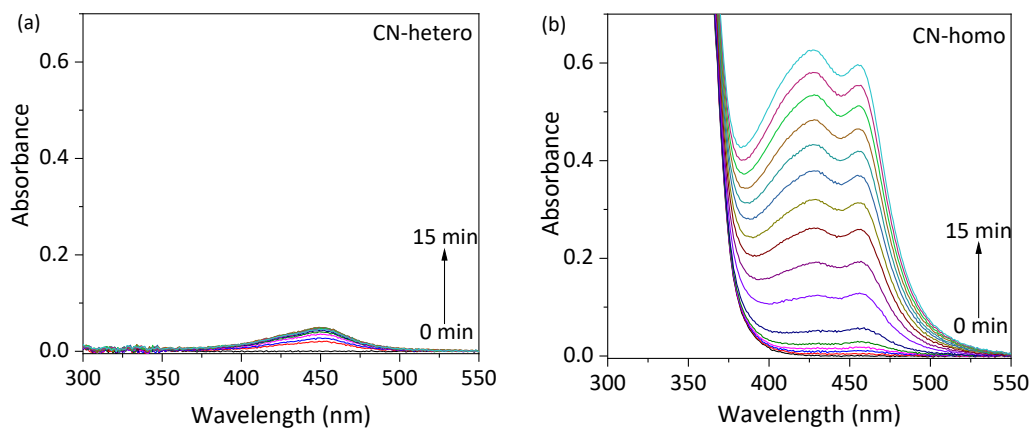


Fig. S11 UV-vis absorption spectra of the reaction mixture for the dehydrogenation of TMB using heterogeneous (CN-hetero, CN dispersed in H₂O) and homogeneous (CN-homo, CN dissolved in MSA) CN photocatalysts at different reaction time.

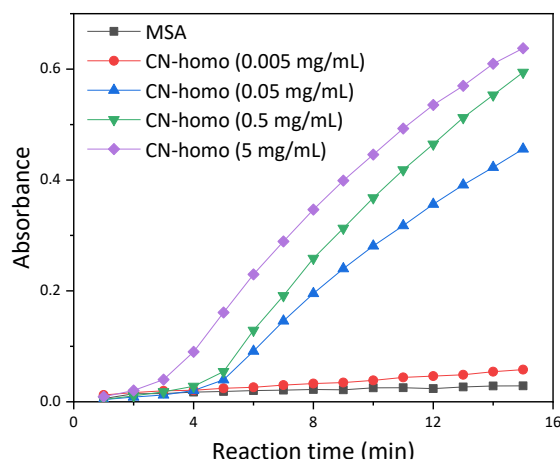


Fig. S12 Absorbance of TMB_{ox} at 456 nm as a function of time during photocatalytic dehydrogenation using MSA and CN-homo catalyst.

As TMB was only dissolvable in acidic aqueous solution, for CN-hetero system, 0.53 M MSA was also added. Moreover, as shown below, when only MSA or a low concentration of CN in MSA was used, the catalytic activity was negligible for CN-homo system. In contrast, when the concentration of CN in MSA increased, the activity increased and gradually reached a plateau. All these facts collaboratively verified that MSA did not significantly affect the catalytic activity. Besides, according to Fig. S12, for a balanced catalytic activity and economics of catalysts, a loading of 0.5 mg/mL was used as an optimal concentration. For a fairer comparison, the heterogeneous system of CN/MSA before the complete dissolution was also explored in photocatalysis, but at a reasonable photocatalyst concentration (0.5 mg/mL), CN dissolved rapidly.

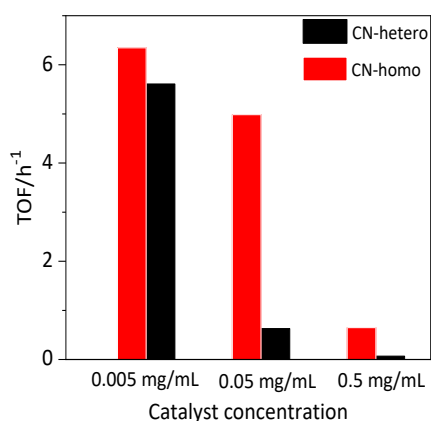


Fig. S13 The turnover frequency (TOF) using CN-hetero (CN dispersed in H₂O) and CN-homo (CN dissolved in MSA) photocatalysts for dehydrogenation of TMB as function of different catalyst concentrations. The TOF was defined by n (TMB) per n (melem units) per hour.¹⁴

In general, the TOF decreases as the loading amount of catalysts increases, and the TOF at sufficient low loading amount of catalysts is often used for theoretic investigation to exclude the concentration effect. Such situation is very similar to the concept of molar conductivity at infinite dilution in physical chemistry (https://en.wikipedia.org/wiki/Molar_conductivity).

When the concentration of CN was sufficient low, the CN-hetero photocatalyst would disperse in the reaction system just like a CN-homo photocatalyst, because all the active sites in both cases were similarly exposed. In this situation, the high TOF indicated the intrinsic activity of the catalyst. Nevertheless, at such low concentration of catalysts, the overall efficiency of the catalytic reaction was low, and virtually useless for practical applications. When the concentration of CN in the reaction system increased in realistic applications, the advantage of CN-homo photocatalyst in exposure of more active sites would gradually become evident. The Fig. S13 and the derived Fig. 3b aimed at the disclosure of these fundamentals and highlighting the evident increase of the catalytic activity due to the dissolution of CN.

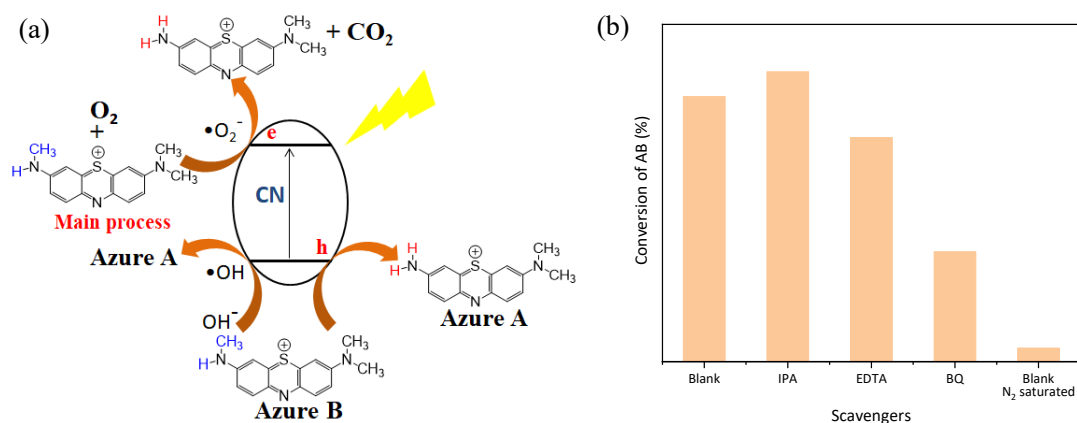


Fig. S14 (a) Proposed mechanism of photocatalytic oxidation of Azure B (AB) into Azure A (AA)¹⁵. (b) The activity changes of photocatalytic N-demethylation of AB by homogeneous CN in MSA after adding different ethylenediamine tetraacetic acid disodium salt (EDTA, 2 mM), isopropanol (IPA, 2 mM), p-benzoquinone (BQ, 2 mM) as scavengers to remove the potential h^+ , •OH, and •O₂⁻, respectively, during the photooxidation reaction.¹³ The conversion of AB significantly decreased after BQ was added, indicating •O₂⁻ was the major species of the reaction. Moreover, it was further verified by the evidently decreased activity in the absence of O₂ by using N₂ saturated solution. In contrast, other scavengers demonstrated minor influences on the photocatalytic activity.

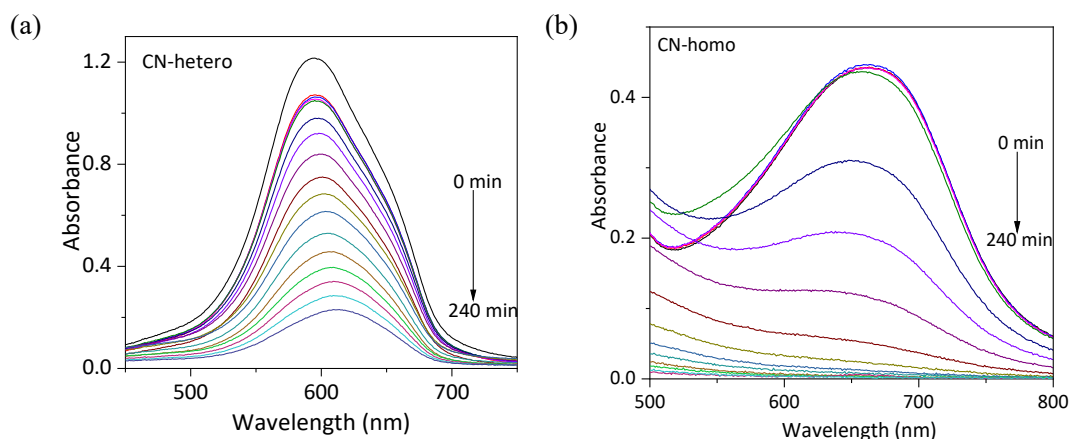


Fig. S15 UV-vis absorption spectra of the reaction mixture for the N-demethylation of AB using CN-hetero (CN dispersed in H₂O) and CN-homo (CN dissolved in MSA) photocatalysts at different reaction time.

The characteristic absorption peak at 594 nm and 660 nm were used to study the kinetics for CN-hetero and CN-homo photocatalytic reactions, respectively.

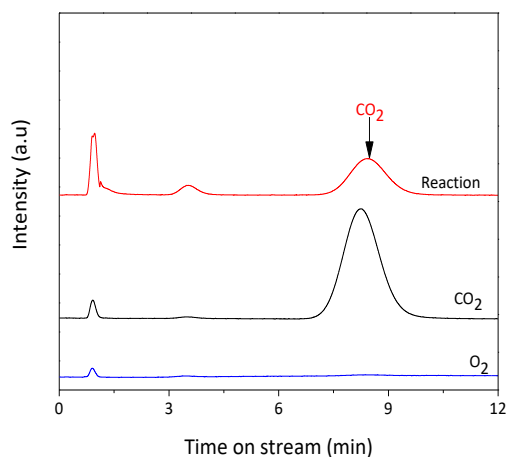


Fig. S16 Gas chromatography spectra of standard O₂, standard CO₂, and the gaseous products of photocatalytic N-demethylation of AB by using CN-homo.

Considering the retention time of the standard O₂ and CO₂, Fig. S16 demonstrated that the gas product of photocatalytic N-demethylation of AB was CO₂ using gas chromatography. To examine the oxidation products quantitatively, the concentration changes of CO₂ was monitored during the AB oxidation. The yield of CO₂ was calculated using the equation of $PV = nRT$ (P : Pa, V : m³, T : K, R : J/mol/K, and n : mol). The results shown after the complete photocatalytic N-demethylation of AB by using CN-homo, the increase mole of CO₂ was ca. 0.8-fold of that of AB. Consisted with the previous reports,^{15b} it indicated that one methyl group of AB was removed after the photocatalytic reaction.

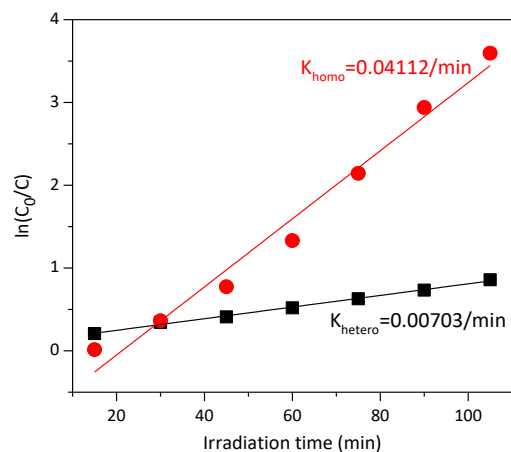


Fig. S17 Plot of $\ln(C_0/C)$ as a function of irradiation time for the N-demethylation of AB using CN-hetero and CN-homo photocatalysts.

For both CN-hetero and CN-homo photocatalysts, the first-order rate constant (k) for the N-demethylation of AB was calculated and shown in Fig. S17. The k of CN-homo catalyst (0.04112/min) was about 6 times of that of CN-hetero catalyst (0.00703/min), indicating a higher activity.

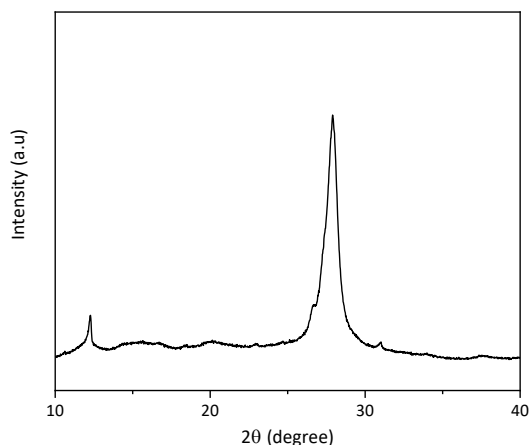


Fig. S18 XRD pattern of r-CN that was recycled from CN-homo after photocatalytic oxidation of AB using ether as the poor solvent.

As shown, r-CN that was obtained from CN-homo after photocatalytic oxidation of AB by using ether as the poor solvent had a high collection yield (ca. 95%) and a similar crystallinity (Fig. S2) to that of the starting bulk CN powders. It suggested a high stability for the CN-homo catalyst in the recycling reaction tests. Moreover, it was noted that in contrast to r-CN of a lower crystallinity that was re-generated by using acetonitrile as the poor solvents (Fig. S2), the precipitation environments (e.g., type of solvents and the co-existence of other species) had a significant impact on the crystallinity of r-CN, which deserves a future study.

Table S2 Comparison of the catalytic dehydrogenation activity of TMB using different catalysts

Sample	Catalyst (mg/mL)	TMB (mg/mL)	Catalytic rate (mg/min)	Reference
CN-homo ^a	0.05	0.15	0.0129	this work
Cu(OH) ₂ ^b	0.06	0.192	0.0427	12
HRP ^b	0.0006	0.192	0.0202	12
AuNPs/Cu-TCP ^b	0.15	0.192	0.0064	16
GO-COOH ^b	0.04	0.192	0.0028	17

^a Upon light irradiation; ^b Using H₂O₂ as the oxidation agent.

Table S3 Comparison of the catalytic activity of N-demethylation of AB using different catalysts

Sample	Concentration (mg/L)	catalytic time (min)	catalytic rate (mg/L/min)	Reference
CN-homo	100	90	1.11	this work
CS TiO ₂	20	20	1.00	¹⁸
P25	20	15	1.33	¹⁸
Fe ²⁺ ^a	9.17	40	0.23	¹⁹
ZnO-RGO	5.2	20	0.26	²⁰
HRP (or LiP) ^a	10	120	0.08	²¹

^a Using H₂O₂ as the oxidation agent instead of upon a light irradiation.

Supporting references:

- (1) Y. Wang; Z. Shi and J. Yin, *J. Mater. Chem.* 2011, **21**, 11371.
- (2) Y. Wang; Z. Shi; J. Fang; H. Xu; X. Ma and J. Yin, *J. Mater. Chem.* 2011, **21**, 505.
- (3) M. J. Frisch, *Gaussian 09, Revision D.01* 2009.
- (4) Y. Zhang; A. Thomas; M. Antonietti and X. Wang, *J. Am. Chem. Soc.* 2009, **131**, 50.
- (5) A. Thomas; A. Fischer; F. Goettmann; M. Antonietti; J.-O. Müller; R. Schlögl and J. M. Carlsson, *J. Mater. Chem.* 2008, **18**, 4893.
- (6) (a) E. G. Gillan, *Chem. Mater.* 2000, **12**; (b) B. I. Jurgens, E.; Senker, J.; Kroll, P.; Muller, H.; Schnick, W., *J. Am. Chem. Soc.* 2003, **125**; (c) X. C. Wang; K. Maeda; A. Thomas; K. Takanahe; G. Xin; J. M. Carlsson; K. Domen and M. Antonietti, *Nat. Mater.* 2009, **8**, 76.
- (7) Y. J. A. Zhang, M., *Chem. Asian. J.* 2010, **5**.
- (8) Z. X. Zhou; J. H. Wang; J. C. Yu; Y. F. Shen; Y. Li; A. R. Liu; S. Q. Liu and Y. J. Zhang, *J. Am. Chem. Soc.* 2015, **137**, 2179.
- (9) M. J. Bojdys; J. O. Muller; M. Antonietti and A. Thomas, *Chem. Eur. J.* 2008, **14**, 8177.
- (10) T. S. Miller; T. M. Suter; A. M. Telford; L. Picco; O. D. Payton; F. Russell-Pavier; P. L. Cullen; A. Sella; M. S. P. Shaffer; J. Nelson; V. Tileli; P. F. McMillan and C. A. Howard, *Nano Lett.* 2017, **17**, 5891.
- (11) X. D. Zhang; X. Xie; H. Wang; J. J. Zhang; B. C. Pan and Y. Xie, *J. Am. Chem. Soc.* 2013, **135**, 18.
- (12) R. Cai; D. Yang; S. J. Peng; X. G. Chen; Y. Huang; Y. Liu; W. J. Hou; S. Y. Yang; Z. B. Liu and W. H. Tan, *J. Am. Chem. Soc.* 2015, **137**, 13957.
- (13) (a) M. C. Yin; Z. S. Li; J. H. Kou and Z. G. Zou, *Environ. Sci. Technol.* 2009, **43**, 8361; (b) L. Sun; W. Hong; J. Liu; M. Yang; W. Lin; G. Chen; D. Yu and X. Chen, *ACS Appl. Mater. Interfaces* 2017, **9**, 44503; (c) Y. Nosaka and A. Y. Nosaka, *Chem. Rev.* 2017, **117**, 11302.
- (14) (a) F. Goettmann; A. Fischer; M. Antonietti and A. Thomas, *Angew. Chem. Int. Ed.* 2006, **45**, 4467; (b) X. F. Chen; J. S. Zhang; X. Z. Fu; M. Antonietti and X. C. Wang, *J. Am. Chem. Soc.* 2009, **131**, 11658.
- (15) (a) L. Alamo-Nole; S. Bailon-Ruiz; T. Luna-Pineda; O. Perales-Perez and F. R. Roman, *J. Mater. Chem. A* 2013, **1**, 5509; (b) E. Akoury; M. Pickhardt; M. Gajda; J. Biernat; E. Mandelkow and M. Zweckstetter, *Angew. Chem. Int. Ed.* 2013, **52**, 3511.
- (16) Y. Huang; M. Zhao; S. Han; Z. Lai; J. Yang; C. Tan; Q. Ma; Q. Lu; J. Chen; X. Zhang; Z. Zhang; B. Li; B. Chen; Y. Zong and H. Zhang, *Adv. Mater.* 2017, **29**.
- (17) Y. Song; K. Qu; C. Zhao; J. Ren and X. Qu, *Adv. Mater.* 2010, **22**, 2206.
- (18) T. Aarathi; P. Narahari and G. Madras, *J. Hazard. Mater.* 2007, **149**, 725.
- (19) A. Aguiar and A. Ferraz, *Chemosphere* 2007, **66**, 947.
- (20) S. Rabieh; K. Nassimi and M. Bagheri, *Mater. Lett.* 2016, **162**, 28.
- (21) V. S. Ferreira-Leitao; J. G. da Silva and E. P. S. Bon, *Appl. Catal. B-Environ.* 2003, **42**, 213.